



### Science Arts & Métiers (SAM)

is an open access repository that collects the work of Arts et Métiers Institute of Technology researchers and makes it freely available over the web where possible.

This is an author-deposited version published in: <https://sam.ensam.eu>  
Handle ID: <http://hdl.handle.net/10985/25481>

#### To cite this version :

Anne-Sophie POUDREL, Max GATTIN, Giuseppe ROSI, Marc RÉBILLAT, Jorge PEIXINHO, Nicolas BOCHUD, Pierre MARGERIT - Identification of viscoelastic material properties by ultrasonic angular measurements in double through-transmission - The Journal of the Acoustical Society of America - Vol. 156, n°1, p.463-474 - 2024

Any correspondence concerning this service should be sent to the repository

Administrator : [scienceouverte@ensam.eu](mailto:scienceouverte@ensam.eu)



# Identification of viscoelastic material properties by ultrasonic angular measurements in double through-transmission

Anne-Sophie Poudrel,<sup>1</sup> Max Gattin,<sup>2</sup> Giuseppe Rosi,<sup>2</sup>  Marc Rébillat,<sup>1</sup> Jorge Peixinho,<sup>1</sup>   
Nicolas Bochud,<sup>2</sup>  and Pierre Margerit<sup>1,a)</sup> 

<sup>1</sup>Laboratoire Procédés et Ingénierie en Mécanique et Matériaux, PIMM, Arts et Métiers ParisTech, UMR 8006, CNRS, CNAM, HESAM université, 151 boulevard de l'hôpital, 75013 Paris, France

<sup>2</sup>Univ Paris Est Creteil, Univ Gustave Eiffel, CNRS, UMR 8208, MSME, F-94010 Créteil, France

## ABSTRACT:

Recent advances in additive manufacturing (AM) of viscoelastic materials have paved the way toward the design of increasingly complex structures. In particular, emerging biomedical applications in acoustics involve structures with periodic micro-architectures, which require a precise knowledge of longitudinal and transverse bulk properties of the constituent materials. However, the identification of the transverse properties of highly soft and attenuating materials remains particularly challenging. Thereby, the present work provides a methodological framework to identify the frequency-dependent ultrasound characteristics (i.e., phase velocity and attenuation) of viscoelastic materials. The proposed approach relies on an inverse procedure based on angular measurements achieved in double through-transmission, referred as  $\theta$ -scan. Toward this goal, a forward modeling of the double transmitted waves through a homogeneous solid is proposed for any incidence angle based on the global matrix formalism. The experimental validation is conducted by performing ultrasound measurements on two types of photopolymers that are commonly employed for AM purposes: a soft elastomer (Elastico™ Black) and a glassy polymer (VeroUltra™ White). As a result, the inferred dispersive ultrasound characteristics are of interest for the computational calibration and validation of models involving complex multi-material structures in the MHz regime.

© 2024 Acoustical Society of America. <https://doi.org/10.1121/10.0026518>

Pages: 463–474

## I. INTRODUCTION

Additive manufacturing (AM), also referred to as three-dimensional (3D) printing, has increasingly expanded over the past decade in engineering and sciences. The development of accurate and versatile 3D printing technologies has paved the way to the design of customized and complex structures printed with a large choice of materials, ranging from elastomers and polymers to ceramics or metals.<sup>1,2</sup> Among these, multi-material jetting, also known as inkjet technology, represents a powerful multi-material 3D printing process, which allows tailoring the material composition from the micro to the macro scale. For instance, this process has not only enabled the fabrication of heterogeneous materials with dissimilar properties,<sup>3</sup> such as periodic lattices or porous media,<sup>4</sup> but has also allowed interpenetrating phase composites<sup>5</sup> or functionally graded materials.<sup>6,7</sup>

In this context, multi-material photopolymer-based AM has experienced a significant interest in acoustics to design and fabricate tailored tissue-mimicking phantoms<sup>8</sup> for calibrating ultrasound imaging systems<sup>9,10</sup> or therapeutic ultrasound applications.<sup>11</sup> Interestingly, the achievement of controlled bio-inspired structures involving periodic micro-architectures has also experienced recent advances to design scaffolds for bone tissue repair.<sup>12</sup> As the prediction of the acoustic behavior of

such structures is particularly challenging, recent modeling efforts have focused on disentangling the relative contributions of viscoelasticity and periodicity on ultrasonic signatures, such as dispersion, attenuation, and bandgaps localization.<sup>13,14</sup> In this respect, an accurate identification of longitudinal and transverse ultrasound characteristics (i.e., phase velocity and attenuation) of the constituent phases is typically required, together with their frequency dependence.

Several ultrasound characterization methods have been explored to measure longitudinal bulk properties of photopolymer materials, including broadband reflection and transmission techniques.<sup>9,10,15</sup> Notwithstanding, only a limited number of works have been performed to report on their transverse properties.<sup>16</sup> Interestingly, the latter study, which relies on the double through-transmission technique, exploits mode conversion at the liquid–solid interface in oblique incidence to measure the transverse properties of the wave propagating inside the material. This approach has been initially developed to measure the phase velocity of anisotropic elastic materials<sup>17,18</sup> and was then extended to the measurement of the attenuation of viscoelastic materials.<sup>19</sup> Although this technique has the advantage to provide longitudinal and transverse bulk properties on a broad frequency range by windowing four measured echoes only (i.e., front-face and back-face reflections at normal incidence, double through-transmission at normal and oblique incidences), it suffers from several drawbacks. First, the

<sup>a)</sup>Email: pierre.margerit@ensam.eu

frequency-thickness product of the sample must be optimized to ensure a proper temporal separation of the echoes. Second, the identification of the transverse bulk properties relies on a measurement performed after the critical angle, above which only transverse waves propagate through the sample. In the case of soft and highly attenuating materials, the critical angle is high and, therefore, the propagation distance is large and, thus, the transverse wave retrieved in double through-transmission is typically drowned in noise. Altogether, these limitations prevent straightforwardly applying the approach described in Ref. 16 to highly viscoelastic materials.

Alternatively, another approach to retrieve the bulk properties of viscoelastic samples relies on the analysis of the reflection and transmission coefficients obtained for different incident angles in simple transmission.<sup>20</sup> An optimization process, performed on the measurement of these coefficients and their modeled counterparts,<sup>21,22</sup> then allows retrieving apparent longitudinal and transverse properties. This approach has been widely applied to anisotropic and viscoelastic materials<sup>23,24</sup> and recently extended to evaluate the anisotropy of adhesive bonds.<sup>25</sup> Unlike that for the *classical* double through-transmission technique, no temporal separation of the echoes is required here. However, the application of this approach to highly viscoelastic materials is not straightforward as the previous studies have not considered dispersive properties. Moreover, only the amplitude of the transmission and reflection coefficients was used in the optimization process, thereby neglecting their phases, which may also carry information on the bulk properties.

Here, we propose to leverage the methodology initially introduced by Ref. 20 on composites, together with the advantages of the double through-transmission technique,<sup>16</sup> to estimate the ultrasound characteristics of photopolymer materials. In particular, the purpose of this work is to provide a methodological framework toward the identification of the frequency-dependent bulk properties of highly viscoelastic materials without the need to isolate the transverse waves after the critical angle. The originality of this work not only lies in the estimation of the longitudinal and transverse phase velocities and attenuations of photopolymer materials but also their frequency dependence as well as the thickness of the sample by considering the complex transmission transfer function in the optimization process. To validate our approach, ultrasound measurements were performed in double through-transmission on viscoelastic samples manufactured using a multi-material 3D printing technology. To this end, several combinations of two dissimilar photopolymers—a glassy polymer and a soft elastomer—were investigated.

The remainder of the paper is organized as follows. Section II describes the additively manufactured samples along with the experimental setup used to achieve the angular measurements in double through-transmission. Then, Sec. III states the principle of the double through-transmission modeling at normal and oblique incidence according to the global matrix formalism, considering the wave amplitude and phase. The optimization strategy for material properties

identification is detailed in Sec. IV. Eventually, the ultrasound characteristics of the photopolymer materials and, in particular, the influence of the volume fraction of each of the two studied materials are reported and discussed in Sec. V.

## II. EXPERIMENTAL METHOD

The proposed ultrasound characterization method relies on the measurement of double through-transmitted signals across the samples at various incident angles, as schematically depicted in Fig. 1. This angular measurement will be referred as *angular scan* in what follows, and its time representation will be named  $\theta$ -scan.

### A. Additively manufactured samples

Multi-material photopolymer samples were achieved using a commercial 3D printer (Polyjet Pro J35, Stratasys, Los Angeles, CA). This AM technology consists of projecting multiple drops of ultraviolet (UV)-curable photopolymer on a building tray through printing nozzles according to a layer-by-layer process.<sup>26</sup> At the microscopic scale (i.e., voxel resolution around  $18\ \mu\text{m}$ ), this inkjet technology allows for the mixing of photopolymers with highly dissimilar viscoelastic properties as a result of the concurrent spreading of multiple streams. At the macroscopic level (i.e., millimetric wavelength in the ultrasound regime), this process results in quasi-homogeneous materials obtained by randomly mixing two contrasted photopolymers.

In this study, two photopolymers were employed: a rigid glassy polymer (commercial name, VeroUltra™ White, denoted by VW) and a soft elastomer (commercial name, Elastico™ Black, denoted by EB). The two pure materials were investigated, 100% of VW (VW100) and 100% of EB (EB100), together with two composite materials, one made of 75% VW and 25% EB (hereinafter called VW75), the other made of 50% of each phase (hereinafter called VW50). The samples were manufactured according

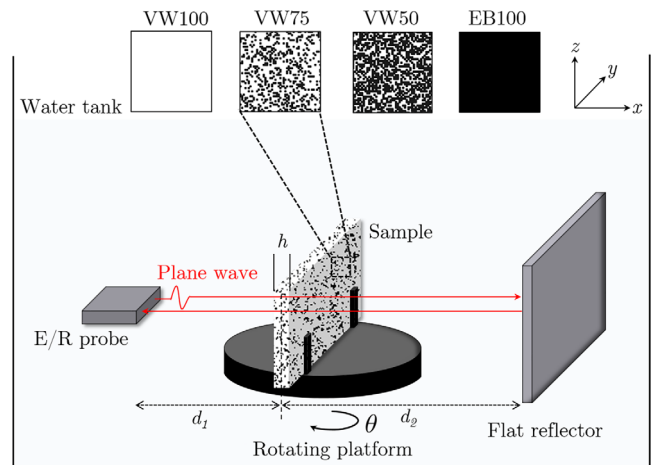


FIG. 1. (Color online) Schematic representation of the experimental setup used for measuring double through-transmitted signals at various incident angles, i.e.,  $0^\circ \leq \theta \leq 64^\circ$ , on photopolymer samples made of VeroUltra™ White (VW) and Elastico™ Black (EB).

to a rectangular plate geometry with overall dimensions of  $35 \times 90 \times h$  mm<sup>3</sup>. The lengths and widths of the samples were selected such that they cover the probe emission surface (recall Fig. 1). The thickness,  $h$ , ranged between 2.5 and 4 mm to ensure a sufficient double through-transmission across the sample for all measurements below the critical angle<sup>27</sup> so as to avoid a too low signal-to-noise ratio (SNR) for the transverse waves because of the attenuation. Note that one sample was manufactured for each material, except for the VW100, for which two samples with two different thicknesses were tested:  $h = 4$  mm (VW100) and  $h = 2.7$  mm (VW100<sub>*t*</sub>). The mass density,  $\rho$ , of each sample was determined from their mass measured with an electronic balance ( $\pm 0.01$  mg) and their dimensions measured with a caliper ( $\pm 0.02$  mm).

## B. Experimental setup

All measurements were performed using a multielement probe (Imasonic SAS, Voray sur l'Ognon, France) connected to a programmable multi-channel electronics system (OEMPA 64/64, Advanced OEM Solutions, West Chester, Ohio), which was driven by MATLAB (The MathWorks Inc., Natick, MA). First developed for medical imaging applications (e.g., elastography<sup>28</sup>), this type of setup was recently used to characterize the bulk properties of homogeneous<sup>16</sup> and heterogeneous photopolymer samples<sup>13,15</sup> in the MHz regime.

The multielement probe consisted of a linear transducer array compound of 32 elements. Each element had a width and height of 0.5 and 12 mm, respectively, leading to a total transmission surface of  $16 \times 12$  mm<sup>2</sup>. The transducer operated at a central frequency,  $f_c = 2.25$  MHz ( $-6$  dB frequency bandwidth from 1.5 to 3 MHz), and the pitch of the array was 0.5 mm. As schematized in Fig. 1, measurements were performed in a water tank using a plane wave imaging mode by concurrently emitting a single Gaussian-modulated sinusoidal pulse on all elements. The received signals,  $s(t)$ , were recorded for  $150 \mu\text{s}$  starting from  $300 \mu\text{s}$  after the pulse emission to selectively observe double through-transmitted waves only using a sampling rate of 100 MHz and a 12-bit resolution. Fresh tap water at room temperature ( $22 \pm 0.5$  °C) was used, and its temperature, which remained constant throughout the experiments, was monitored by a digital thermometer (LCD digital thermometer, resolution of  $\pm 0.1$  °C), such that the water celerity could be estimated using the polynomial model by Marczak.<sup>29</sup>

The advantages of using a multielement probe as emitter and receiver rather than a mono-element probe are twofold. First, as the wavelength in water at the central frequency was small compared to the lateral dimension of the probe array, a high directivity factor was assumed and, thus, geometrical diffraction effects could be neglected in the further processing and modeling of the double through-transmitted signals. Second, the recorded signals could be averaged over the 32 elements of the probe, thus, enhancing the SNR of the measurement.<sup>16</sup> To retrieve double through-transmitted waves, a flat reflector consisting of a custom-

made rectangular aluminum block of  $100 \times 100 \times 48$  mm<sup>3</sup> was used, which was oriented parallel to the transducer. In this configuration, the backward propagating plane waves travel exactly along the same path as the forward incident wave.<sup>18</sup> Thereby, the transducer remains fixed regardless of the incident angle, whereas in simple through-transmission, the receiver has to be shifted depending on the angle of the incident wave.<sup>17,20</sup> Another advantage of double through-transmission is to reduce the amplitude differences between the various waves being compared, which is of paramount importance for transverse wave measurement in highly attenuating materials, where this amplitude difference could be in the same order of magnitude as the dynamic range of the transducer, leading to weak SNR or signal distortion.

The samples were mounted on a motorized rotation stage ( $\pm 1^\circ$ ), and the signals,  $s(t)$ , were recorded for each incident angle,  $\theta$ , between  $0^\circ$  and  $64^\circ$  with a  $1^\circ$  step. The starting position corresponding to the normal incidence (i.e.,  $\theta = 0^\circ$ ) was defined such that the transducer array, sample, and reflector faces were all parallel. To do so, an alignment procedure was applied first between the transducer array and reflector. The optimal azimuthal alignment (i.e., around the  $z$  axis; see Fig. 1) was achieved by minimizing the time-of-flight difference between the front-face reflected signals received on the leftmost and rightmost array's elements. Second, the vertical alignment (i.e., around the  $y$  axis; see Fig. 1), was obtained by maximizing the SNR of the reflected signals. The same procedure was then applied between the transducer array and the sample by rotating the sample only. Eventually, the double through-transmitted wave across the water only, denoted by  $s_{\text{ref}}(t)$ , was measured by removing the sample without moving the transducer and flat reflector. To evaluate the reproducibility of the measurement (e.g., probe-sample-mirror alignment and parallelism of the sample's faces), the full *angular scan* measurement was repeated three times on the VW100 sample.

Three examples of experimental  $\theta$ -scans are displayed in Fig. 2 for the following materials: (a) VW100, (b) VW50, and (c) EB100, together with the temporal signals,  $s(t)$ , obtained at three specific incident angles, i.e.,  $\theta = 0^\circ$ ,  $30^\circ$ , and  $60^\circ$ . As can be observed, the critical angle is visible on each  $\theta$ -scan at the angle for which the signal vanishes, and its value increases when the volume fraction of VW decreases. In addition, while the transverse wave is clearly visible after the critical angle for the VW100 sample [see Figs. 2(a) and 2(d) at  $\theta = 60^\circ$ ], its amplitude is much lower for the VW50 sample [see Figs. 2(b) and 2(e) at  $\theta = 60^\circ$ ] and totally drowned in noise for the EB100 sample [see Figs. 2(c) and 2(f) at  $\theta = 60^\circ$ ]. These observations support the need of a specific methodology to retrieve the transverse properties of such attenuating materials.

## III. DOUBLE THROUGH-TRANSMISSION MODELING

We consider the double through-transmission (forward path, reflection on a mirror, then backward path<sup>18</sup>) of a plane harmonic acoustic wave with angular frequency,  $\omega$ , and incidence angle,  $\theta$ , through a homogeneous and isotropic

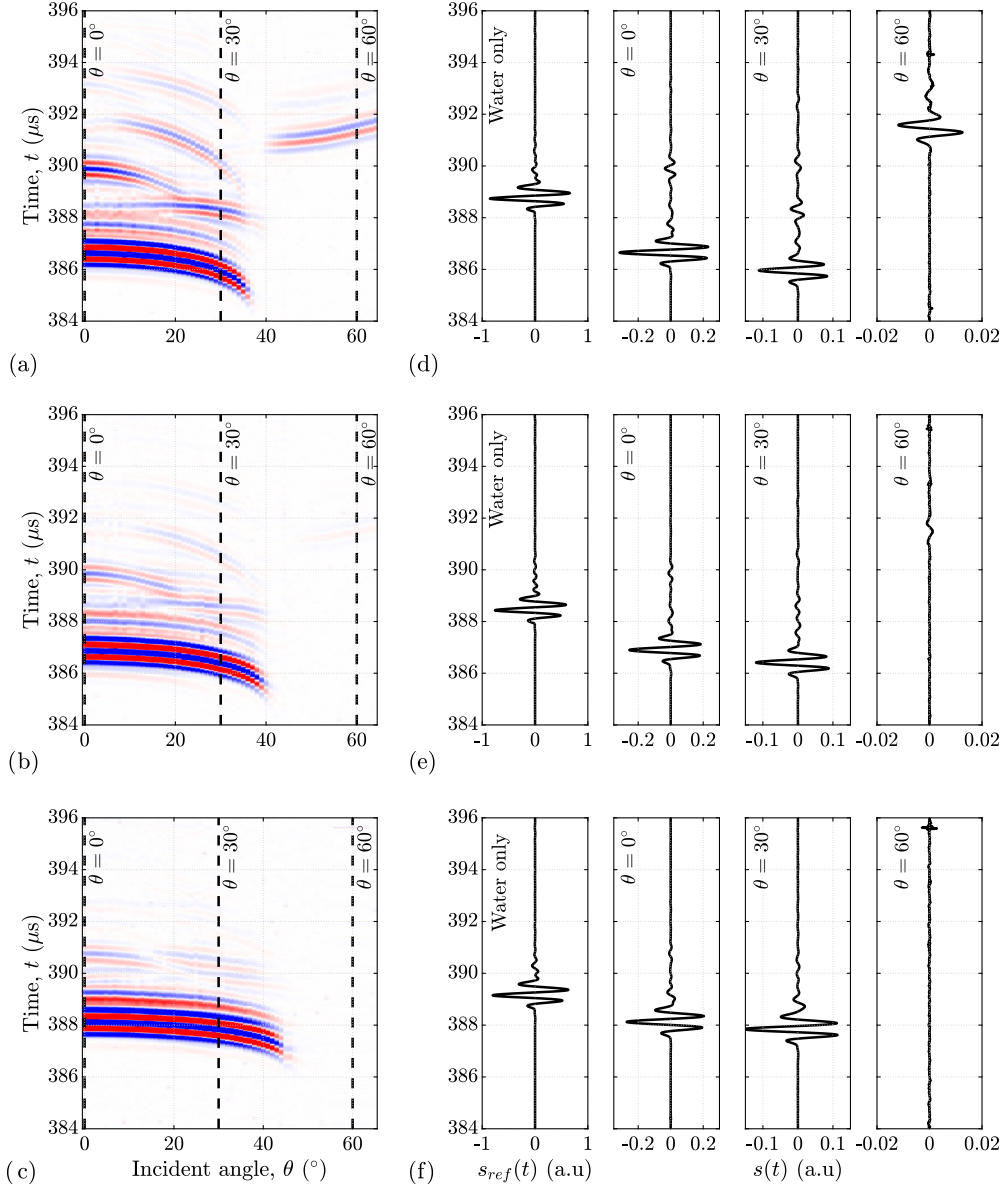


FIG. 2. (Color online) Examples of experimental  $\theta$ -scans of double through-transmitted signals measured on (a) VW100, (b) VW50, and (c) EB100 samples, along with their respective signal displacements,  $s(t)$  [(d), (e) and (f), respectively] obtained in water only [i.e.,  $s_{\text{ref}}(t)$ ] and at three specific incident angles,  $\theta = 0^\circ$ ,  $30^\circ$  and  $60^\circ$ . The saturated colormap for each  $\theta$ -scan represents the normalized positive (in red) and negative (in blue) amplitudes of the signals. It is worth noting that the strong amplitude decrease in the signals retrieved after the critical angle at  $\theta = 60^\circ$ , in particular, for (e) VW50 and (f) EB100.

solid material (mass density,  $\rho$ , and longitudinal and transverse wave numbers,  $k_\ell$  and  $k_t$ , respectively) immersed in a fluid (mass density,  $\rho_0$ , and wave number,  $k_0$ ). The mirror surface is assumed to be normal to the acoustic wavevector,  $\mathbf{k}_0 = k_0 [\cos \theta \ \sin \theta]$ , such that the forward and backward paths are *symmetrical*.

The method relies on the relation between the double through-transmitted signals measured *with* the sample inserted and *without* it (so-called insertion/substitution method<sup>30</sup>). These are, respectively, denoted by  $S(\omega)$  and  $S_{\text{ref}}(\omega)$  as the Fourier coefficients of  $s(t)$  and  $s_{\text{ref}}(t)$  at the frequency,  $\omega$ . Dropping the dependence of all variables on  $\omega$ , such relation can be expressed as

$$S = H_T^2 S_{\text{ref}}, \quad (1)$$

where

$$S_{\text{ref}} = S_{\text{in}} \overbrace{P(d_1 + d_2)}^{\text{forward}} \underbrace{R}_{\text{reflection}} \overbrace{P(d_2 + d_1)}^{\text{backward}}, \quad (2)$$

and

$$S = S_{\text{in}} \overbrace{P(d_1) \underbrace{H_T}_{\text{transmission}} P(d_2)}^{\text{forward}} \underbrace{R}_{\text{reflection}} \overbrace{\times P(d_2) \underbrace{H_T}_{\text{transmission}} P(d_1)}^{\text{backward}}, \quad (3)$$

where  $S_{\text{in}}$  is the complex spectrum of the input signal,  $P(d_i) = e^{-ik_0 d_i}$  is the propagation *phase* associated with the fluid path,  $d_i$ , where  $i = 1, 2$ ,  $R$  is the transfer function associated with the reflection on the mirror, and  $H_{\text{T}}$  is the transfer function corresponding to the *single* transmission of waves through the specimen. The distances,  $d_1$  and  $d_2$ , correspond to the probe-sample and sample-mirror distances, respectively, as depicted in Fig. 1. These are defined with respect to *the plane of symmetry of the sample*, such that  $H_{\text{T}}$  already takes into account the phase,  $P(-h)$ , which is associated with the insertion of the sample in the propagating path.

It is, thus, clear that measuring the reference signal,  $s_{\text{ref}}(t)$ , presents several advantages: the transfer function,  $H_{\text{T}}$ , can be estimated experimentally and used as the basis for the identification of the sample properties without prior knowledge of the distances,  $d_1$  and  $d_2$ , the input signal,  $S_{\text{in}}$ , and, more interestingly, the mirror reflection transfer function,  $R$ . Hence, the mirror can be of arbitrary material and/or thickness<sup>17</sup> without constraint associated with the time separation of the successive trains of echoes.

### A. Single transmission transfer function

As the relation between  $S$  and  $S_{\text{ref}}$  only involves the squared transfer function,  $H_{\text{T}}$ , the model of the experimental data is reduced to the calculation of the *single wave transmission* that corresponds to the problem statement shown in Fig. 3. We, therefore, derive  $H_{\text{T}}$  as the ratio between the transmitted and incident complex wave amplitudes, respectively, denoted by  $a_{\text{T}}$  and  $a_{\text{I}}$ , for any incident angle,  $\theta$ , and frequency,  $\omega$ . Note that  $a_{\text{R}}$  stands for the reflected complex wave amplitude. The two-dimensional (2D) coordinate system  $(x, y)$  is chosen such that the two infinite solid–fluid plane interfaces are situated at  $x = \pm h/2$ , and their normal is along  $x$ . Hence, all wave phases are expressed *with respect* to the solid layer plane of symmetry at  $x = 0$ .

In each subdomain, the pressure field,  $p$ , or displacement field,  $\mathbf{u}$ , is assumed as a combination of plane waves with amplitudes,  $a_r$ , polarizations,  $\mathcal{P}^{(r)}$  or  $\mathcal{U}^{(r)}$ , and wavevector,  $\mathbf{k}_r = [\xi_r \ \kappa_r] = k_r [\cos \theta_r \ \sin \theta_r]$  as

$$\begin{bmatrix} \mathbf{u}(x, y) \\ p(x, y) \end{bmatrix} = \sum_r a_r \begin{bmatrix} \mathcal{U}^{(r)} \\ \mathcal{P}^{(r)} \end{bmatrix} e^{-i(\xi_r x + \kappa_r y)}, \quad (4)$$

where  $r$  stands either for the wave propagating in water ( $r = 0$ ) or the *longitudinal* ( $r = \ell$ ) and *transverse* ( $r = t$ ) waves in the solid.

The relation between wave amplitudes is governed by the continuity of the stress vector,  $(\sigma_{xx}, \sigma_{xy})$ , and normal displacements,  $u_x$ , at both solid–fluid interfaces, which can be expressed as

$$\sigma_{xx} \left( x = \pm \frac{h}{2}, y \right) + p \left( x = \pm \frac{h}{2}, y \right) = 0, \quad (5a)$$

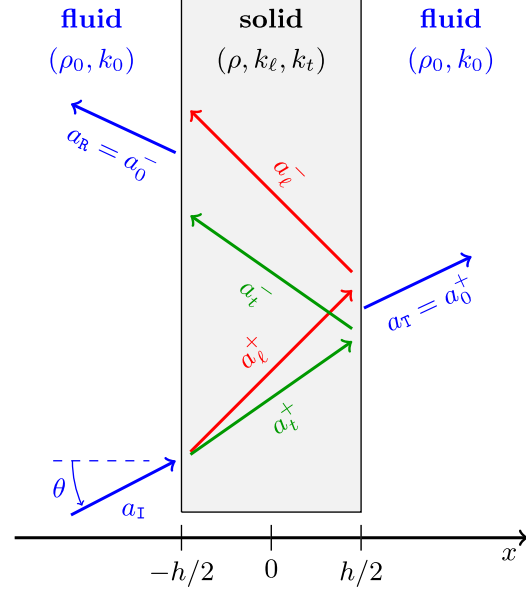


FIG. 3. (Color online) Scheme of the single wave transmission problem, where  $a_{\text{I}}$ ,  $a_{\text{T}}$ , and  $a_{\text{R}}$  are the incident, transmitted, and reflected complex wave amplitudes, respectively. Forward and backward waves are denoted by the superscript “ $\pm$ .”

$$\sigma_{xy} \left( x = \pm \frac{h}{2}, y \right) = 0, \quad (5b)$$

$$\rho_0 \omega^2 u_x \left( x = \pm \frac{h}{2}, y \right) - \frac{\partial}{\partial x} p \left( x = \pm \frac{h}{2}, y \right) = 0. \quad (5c)$$

As these six continuity equations need to be fulfilled for any  $y$ , the wave modulation,  $e^{-i\kappa_r y}$ , along the vertical axis must be constant across interfaces. This leads to the well-known Snell-Descartes law as

$$\kappa_r = k_r \sin \theta_r = k_0 \sin \theta = \kappa, \quad \forall r, \quad (6)$$

where  $\kappa$  is the *vertical* component of the wavevector, which is a constant of the problem. It is worth noting that the wavevectors,  $\mathbf{k}_r$ , are generally complex and can have non-colinear real and imaginary parts; thus, the angles  $\theta_r$  can take complex values in general. Here, it is chosen to derive the following expressions using the wavevector components  $(\xi_r, \kappa)$ . In particular, the *absolute* projection of  $\chi_r$  of the wavevectors on the  $x$  axis, such that  $\xi_r = \pm \chi_r$ , relates to either the *forward* (+) or *backward* (−) paths as denoted in Fig. 3, and is defined as

$$\chi_r = \sqrt{k_r^2 - \kappa^2}, \quad (7)$$

where  $\chi_r$  may take complex values when  $|k_r| < |\kappa|$ .

The six continuity equations in Eq. (5) can then be recast following a global matrix formalism<sup>31</sup> (see Appendix A). By taking into account the symmetries of the fluid–solid interfaces and forward-backward waves, the matrix can be recast to obtain two decoupled  $3 \times 3$  systems, which can be

subsequently analytically inverted to recover the expressions of  $a_0^S$  and  $a_0^A$ , such that  $a_r^\pm = a_r^S \pm a_r^A$ , where the superscripts  $A$  and  $S$  stand for antisymmetric and symmetric parts, respectively. At the end, using the fact that  $a_T = a_0^+ = a_0^S + a_0^A$ , the analytical expression of the complex transfer function associated with the single wave *transmission*,  $H_T$ , through the solid domain reads as

$$H_T = \frac{a_T}{a_I} = -4 \frac{\gamma \alpha \Pi_\ell (\Pi_\ell^2 - 1) + \beta \Pi_t (\Pi_\ell^2 - 1)}{\Pi_0 \Delta}, \quad (8)$$

where

$$\begin{aligned} \Delta = & (\alpha + \beta - \gamma)^2 (\Pi_\ell^2 - 1) (\Pi_t^2 - 1) \\ & - 4\beta\gamma (\Pi_\ell^2 - 1) - 4\alpha\gamma (\Pi_t^2 - 1) \\ & + 4\alpha\beta (\Pi_\ell - \Pi_t)^2, \end{aligned} \quad (9a)$$

$$\Pi_r = e^{-i\chi_r h}, \quad (9b)$$

$$\alpha = (\chi_t^2 - \kappa^2)^2, \quad (9c)$$

$$\beta = 4\kappa^2 \chi_\ell \chi_t, \quad (9d)$$

$$\gamma = \frac{\rho_0 \chi_\ell}{\rho \chi_0} (\chi_t^2 + \kappa^2)^2. \quad (9e)$$

## B. Frequency dependence of the wave number

The single transmission transfer function,  $H_T$ , given by Eq. (8), can be used to compute, the  $\theta$ -scan corresponding to a sample with given wave dispersion characteristics, from Eq. (1) and the measured reference signal,  $s_{\text{ref}}(t)$ . In other words, the dependence of  $k_0$ ,  $k_\ell$ , and  $k_t$  with the frequency,  $\omega$ , needs to be provided to predict the double through-transmitted signal,  $s(t)$ . In the following, we use the general formulation

$$k_r(\omega) = \frac{\omega}{v_r(\omega)} - i \alpha_r(\omega), \quad (10)$$

where  $v_r(\omega)$  and  $\alpha_r(\omega)$ , respectively, denote the phase velocity and attenuation as *real* functions of the frequency.

### 1. Nondispersive media

As a starting point, nondispersive properties can be assumed for the solid and fluid media, characterized with a *complex* and *constant* wave celerity,  $c_r \in \mathbb{C}$ , such that  $k_r(\omega) = \omega/c_r$ . Hence,

$$v_r(\omega) = \Re(c_r) \left( 1 + \frac{\Im(c_r)^2}{\Re(c_r)^2} \right) \quad \text{and} \quad \alpha_r(\omega) = \omega \frac{\Im(c_r)}{|c_r|^2}. \quad (11)$$

This assumption is known to provide a good approximation for the wave number,  $k_0$ , which is associated with pressure waves in the fluid. In particular, as the temperature is known, the wave celerity,  $c_0$ , in water can be predicted using

the polynomial model by Marczak.<sup>29</sup> In this work, the non-dispersive model from Eq. (11) is also used to provide an initialization for the material wave numbers,  $(k_\ell, k_t)$ , required in the inverse problem (see Sec. IV A).

## 2. Szabo's rheological model

Viscoelastic materials, such as photopolymers, exhibit dispersive losses that cannot be accurately captured by a classical rheological Voigt model (i.e., attenuation proportional to  $\omega^2$ ), which may be caused by their heterogeneous nature involving multiple relaxation mechanisms. Nevertheless, earlier studies by our group<sup>15,16</sup> evidenced that the viscoelastic behavior of photopolymers may be well described by the Szabos model.<sup>32</sup> This phenomenological model has the advantage to describe not only the frequency dependence of the attenuation,  $\alpha_r(\omega)$ , with a power-law but also the frequency variations of the phase velocity,  $v_r(\omega)$ , because the model is causal in the sense that it satisfies Kramer-Kronig relationships.<sup>33</sup> In this regard, convenient expressions of  $v_r(\omega)$  and  $\alpha_r(\omega)$  as a function of a reference frequency,  $\omega_c$ , were proposed by Ref. 10 as

$$v_r(\omega) = \left( \frac{1}{v_{cr}} + \frac{\alpha_{cr}}{\omega_c} \tan\left(\frac{\pi}{2} y_r\right) \left( \frac{\omega}{\omega_c} \right)^{y_r-1} - 1 \right)^{-1}, \quad (12a)$$

$$\alpha_r(\omega) = \alpha_{cr} \left( \frac{\omega}{\omega_c} \right)^{y_r}, \quad (12b)$$

where  $\omega_c = 2\pi f_c$  can be deliberately chosen as the central frequency of the available ultrasonic probe. With the Szabo model, the dependence of the wave number,  $k_r(\omega)$ , with the frequency is, thus, completely given by the three corresponding parameters,  $v_{cr}$ ,  $\alpha_{cr}$ , and  $y_r$ , which denote the phase velocity and attenuation at the central frequency,  $\omega_c$ , and a dispersion coefficient, respectively.

## IV. IDENTIFICATION OF VISCOELASTIC MATERIAL PROPERTIES

The inverse procedure used to identify the ultrasound characteristics [phase velocity,  $v_r(\omega)$ , and attenuation,  $\alpha_r(\omega)$ ] from a measured  $\theta$ -scan,  $s(t, \theta)$ , the reference signal,  $s_{\text{ref}}(t)$ , and the model,  $H_T(\omega, \theta)$ , are described in what follows. In practice, the wave dispersion,  $k_r(\omega)$ , needs to be given on the whole frequency domain to reconstruct a *candidate*  $\theta$ -scan using Eq. (1). However, the ultrasound probe is characterized by a *limited* bandwidth around  $\omega_c$ . Thereby, a rheological model, such as Eq. (11) or Eq. (12), is used to regularize the inverse problem. In particular, the procedure is here divided into two steps.<sup>34</sup> First, an initial *guess* is provided using the estimation of a nondispersive longitudinal celerity,  $c_\ell$ , via a direct problem. Second, an optimization procedure is implemented to estimate the model parameters of the Szabo model.

## A. Calibration of the model at normal incidence

For a normally incident plane wave ( $\theta = 0$ ), the vertical component of the wavevector vanishes, thus,  $\kappa = 0$ . Consequently, the expression of  $H_T$  in Eq. (8) can be simplified to

$$H_T = \frac{T_\ell^2}{\Pi_0} (\Pi_\ell^{-1} - R_\ell^2 \Pi_\ell)^{-1}, \quad (13)$$

where

$$T_\ell = \frac{2\zeta_\ell}{\zeta_\ell + 1}, \quad R_\ell = \frac{\zeta_\ell - 1}{\zeta_\ell + 1}, \quad \text{and} \quad \zeta_\ell = \frac{\rho}{\rho_0} \frac{k_0}{k_\ell}.$$

Under the hypothesis of a *nondispersive* material behavior [recall Eq. (11)], it is noteworthy that  $\zeta_\ell$ , thus  $T_\ell$  and  $R_\ell$ , are constants. In such a case, this allows us to express the inverse of the double through-transmission transfer function as

$$\frac{S_{\text{ref}}(\omega)}{S(\omega)} = [H_T(\omega)]^{-2} = \frac{\psi_0^\omega}{T_\ell^4} (\psi_\ell^{-\omega} - 2R_\ell^2 + R_\ell^4 \psi_\ell^\omega), \quad (14)$$

where  $\psi_r = e^{-i2h/c_r}$ . Once the above expression is multiplied by  $\psi_0^{-\omega}$ , which can be computed from the wave celerity,  $c_0$ , in water and specimen thickness,  $h$ , it takes the form of a harmonic polynomial in  $\psi_\ell$  only. Hence, a Prony method is implemented here to provide an initial guess of the longitudinal wave number,  $k_\ell$ , associated with a constant celerity,  $c_\ell \in \mathbb{C}$  (see Appendix B).

## B. Estimation of dispersive properties

We propose an optimization procedure based on the full  $\theta$ -scan to identify, for each sample, the parameters of the Szabo model [recall Eq. (12)], i.e.,  $\mathbf{p}_r = [v_{cr}, \alpha_{cr}]$  associated with longitudinal ( $r = \ell$ ) and transverse ( $r = t$ ) waves. Note that the dispersion coefficient,  $y_r$ , involved in Szabo's model is assumed to be equal to  $y_\ell = 1.1$  and  $y_t = 0.7$  for all the investigated materials based on the results obtained in Refs. 15 and 16. In addition, the sample thickness,  $h$ , and a uniform angle correction,  $\theta_0$ , which may be interpreted as an experimental angle offset at the normal incidence, are included as *refinement* parameters to avoid biases due to their experimental initial determination. The set of parameters,  $\mathbf{p} = [\mathbf{p}_\ell, \mathbf{p}_t]$ , is, thus, estimated via the following minimization problem:

$$(\hat{\mathbf{p}}, \hat{h}, \hat{\theta}_0) = \arg \min_{\substack{\mathbf{p} \in \mathbb{R}^4 \\ h \in \mathbb{R} \\ \theta_0 \in \mathbb{R}}} \sum_{t_i, \theta_j} \Delta s(t_i, \theta_j; \mathbf{p}, h, \theta_0)^2, \quad (15)$$

where the residual,  $\Delta s$ , is given by

$$\Delta s(t, \theta; \mathbf{p}, h, \theta_0) = u(t, \theta; \mathbf{p}, h, \theta_0) - s(t, \theta), \quad (16)$$

and the signal *model*,  $u$ , is computed as

$$u(t, \theta; \mathbf{p}, h, \theta_0) = \mathcal{F}^{-1}[H_T(\omega, \theta + \theta_0; \mathbf{p}, h) S_{\text{ref}}(\omega)], \quad (17)$$

where  $\mathcal{F}^{-1}$  denotes the inverse Fourier transform. In contrast to an estimation that would be based on the transfer function only, performing the minimization directly on the temporal data,  $s(t, \theta)$ , provides a natural *weighting* of the error, associated with the reference signal,  $s_{\text{ref}}$ , which accounts for the probe's bandwidth and losses/reflections in the mirror.

The optimization procedure was implemented using a gradient-based method implemented in MATLAB (The MathWorks Inc., Natick, MA) and finite differences for the numerical estimation of the gradient of the residuals.

As required by such an approach, a specific initialization of the set of model parameters,  $\mathbf{p}$ , was performed. The longitudinal parameters of the Szabo model,  $\mathbf{p}_\ell$ , were initialized from the longitudinal wave number,  $k_\ell$ , which is associated with the constant complex velocity,  $c_\ell$ , estimated at the normal incidence using the model calibration described in Sec. IV A. Likewise, the initialization of the transverse parameters,  $\mathbf{p}_t$ , was subsequently determined from the complex transverse wave celerity,  $c_t$ , which can be determined from the relation

$$c_t = c_\ell \sqrt{\frac{1 - 2\nu_i}{2(1 - \nu_i)}}, \quad (18)$$

assuming an *initial* Poisson's ratio,  $\nu_i$ , equal to 0.38 for all samples.<sup>16</sup> Eventually, the angle correction,  $\theta_0$ , was arbitrary initialized to  $0.01^\circ$ , which corresponds to the uncertainty of the rotating platform, and the sample thickness,  $h$ , was initialized to the experimental value measured with a caliper, as described in Sec. II.

To serve as an example, Fig. 4 depicts the optimal matching between the measured and modeled  $\theta$ -scans for the VW100 sample. As can be observed, the measured and modeled signals are in excellent agreement, which is revealed herein for three specific incidence angles,  $\theta$ .

## C. Uncertainty of the identification procedure

The uncertainty associated with the inverse procedure, noted  $\sigma_{\hat{\mathbf{p}}}$ , was evaluated via error propagation for the set of parameter,  $\hat{\mathbf{p}}$ , assuming independent variables, as

$$\sigma_{\hat{p}_k} = \sqrt{\sum_{t_i, \theta_j} \left( \frac{\partial p_k}{\partial u} \Big|_{(t_i, \theta_j; \hat{\mathbf{p}}, \hat{h}, \hat{\theta}_0)} \right)^2 \Delta s(t_i, \theta_j; \hat{\mathbf{p}}, \hat{h}, \hat{\theta}_0)^2}, \quad (19)$$

where the terms between parentheses are obtained via an inversion of the model sensitivity matrix. At the end, each parameter is associated with a confidence interval of 95% such that  $p_k \pm 1.96 \sigma_{\hat{p}_k}$ .

## V. RESULTS

The optimized Szabo parameters,  $\mathbf{p}_r = [v_{cr}, \alpha_{cr}]$  for  $r = \{\ell, t\}$ , as defined in Sec. IV B, are reported in Table I for



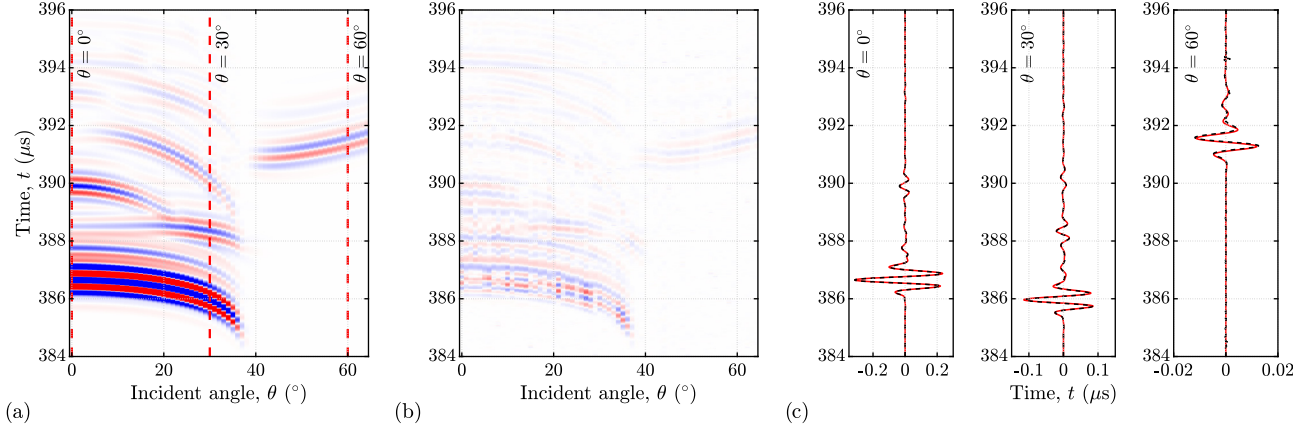


FIG. 4. (Color online) Illustration of the optimization procedure applied to one realization of the VW100 sample. (a) Modeled  $\theta$ -scan obtained with the optimized set of parameters,  $\hat{\mathbf{p}}$ , (b) difference between the experimental  $\theta$ -scan shown in Fig. 2(a) and the modeled  $\theta$ -scan, and (c) comparison of experimental (black line) and modeled (red line) double through-transmitted signals at three specific incident angles  $\theta = 0^\circ$ ,  $30^\circ$ , and  $60^\circ$  are displayed. The experimental signals (black line) correspond to those displayed in Fig. 2(d). The colormaps of (a) and (b) are ten times saturated to highlight the successive echoes arising from the mode conversion at the interfaces.

all samples, together with the optimized sample thickness,  $\hat{h}$ , and the uniform incident angle correction,  $\hat{\theta}_0$ . All values are given with their respective uncertainty, which is related to the identification procedure as explained in Sec. IV C.

### A. Measurement reproducibility

The ultrasound characteristics of VW are displayed in Fig. 5 for three independent measurements performed on the same sample, along with a measurement performed on a thinner sample.

On one hand, at the probe's central frequency, i.e.,  $f_c = 2.25$  MHz, some discrepancies can be observed across the three measurement repetitions. While the optimized longitudinal phase velocity,  $\hat{v}_{cl}$ , varies between  $2423.0 \pm 0.5$  m/s and  $2447.4 \pm 0.2$  m/s, the transverse phase velocity,  $\hat{v}_{ct}$ , varies between  $1097.9 \pm 0.3$  m/s and  $1113.7 \pm 0.1$  m/s, which represents less than 2% of relative error. Comparable results are obtained for the attenuation, where the optimized

longitudinal attenuation,  $\hat{\alpha}_{cl}$  (respectively, transverse attenuation,  $\hat{\alpha}_{ct}$ ), ranges between  $8.31 \pm 0.01$  dB/cm and  $8.69 \pm 0.04$  dB/cm (respectively, between  $37.9 \pm 0.1$  dB/cm and  $36.2 \pm 0.1$  dB/cm), which represents a relative error of about 5%.

On the other hand, although the results obtained on the two samples of VW, termed VW100 and VW100, in Table I, are in relatively good quantitative agreement, the overall optimized Szabo's parameters,  $[\mathbf{p}_\ell, \mathbf{p}_t]$ , are slightly higher for the thinner sample. These variations across the samples and measurements will be further discussed in Sec. VI.

### B. Influence of the material mixing

The influence of the volume fraction,  $V_f$ , of VW on the frequency-dependent ultrasound characteristics is depicted in Fig. 6 for  $V_f = 100\%$ ,  $75\%$ ,  $50\%$ , and  $0\%$ , recalling that  $0\%$  corresponds to the pure soft elastomer, named EB100. For the

TABLE I. Measured mass density,  $\rho$ , and optimized ultrasound parameters,  $\hat{\mathbf{p}} = [\hat{v}_{cr}, \hat{\alpha}_{cr}, \hat{\theta}_0, \hat{h}]$ . For each quantity, the uncertainty associated with the measurement (for  $\rho$ ) or inverse method (for  $\hat{\mathbf{p}}$ ) is indicated with 96% of confidence for the latter.

|        | $\rho$ (kg/m <sup>3</sup> ) | Measure number | $\hat{\theta}_0$ (°) | $\hat{h}$ (mm)  | $r$    | $\hat{v}_{cr}$ (m/s) | $\hat{\alpha}_{cr}$ (dB/cm) |
|--------|-----------------------------|----------------|----------------------|-----------------|--------|----------------------|-----------------------------|
| VW100  | $1185.3 \pm 0.5$            | 1              | $0.14 \pm 0.01$      | $3.98 \pm 0.00$ | $\ell$ | $2447.4 \pm 0.2$     | $8.31 \pm 0.01$             |
|        |                             |                |                      |                 | $t$    | $1113.7 \pm 0.1$     | $36.2 \pm 0.1$              |
|        |                             | 2              | $0.03 \pm 0.03$      | $3.93 \pm 0.00$ | $\ell$ | $2433.1 \pm 0.9$     | $8.69 \pm 0.04$             |
|        |                             |                |                      |                 | $t$    | $1097.9 \pm 0.3$     | $37.8 \pm 0.11$             |
|        |                             | 3              | $0.28 \pm 0.02$      | $3.93 \pm 0.00$ | $\ell$ | $2423.0 \pm 0.5$     | $8.63 \pm 0.02$             |
|        |                             |                |                      |                 | $t$    | $1101.5 \pm 0.2$     | $37.9 \pm 0.1$              |
| VW100, | $1185.3 \pm 0.5$            | 1              | $0.64 \pm 0.07$      | $2.76 \pm 0.01$ | $\ell$ | $2464.7 \pm 1.7$     | $8.25 \pm 0.11$             |
|        |                             |                |                      |                 | $t$    | $1134.2 \pm 0.4$     | $40.1 \pm 0.1$              |
| VW75   | $1162.9 \pm 0.4$            | 1              | $0.01 \pm 0.02$      | $3.67 \pm 0.00$ | $\ell$ | $2379.5 \pm 0.3$     | $9.50 \pm 0.02$             |
|        |                             |                |                      |                 | $t$    | $1069.1 \pm 0.2$     | $47.2 \pm 0.2$              |
| VW50   | $1147.9 \pm 0.7$            | 1              | $1.16 \pm 0.02$      | $3.39 \pm 0.01$ | $\ell$ | $2255.8 \pm 0.6$     | $11.5 \pm 0.1$              |
|        |                             |                |                      |                 | $t$    | $991.4 \pm 1.0$      | $69.3 \pm 0.8$              |
| EB100  | $1115.1 \pm 0.8$            | 1              | $1.24 \pm 0.03$      | $2.78 \pm 0.01$ | $\ell$ | $2035.1 \pm 0.9$     | $15.4 \pm 0.03$             |
|        |                             |                |                      |                 | $t$    | $740.6 \pm 0.8$      | $86.3 \pm 1.5$              |

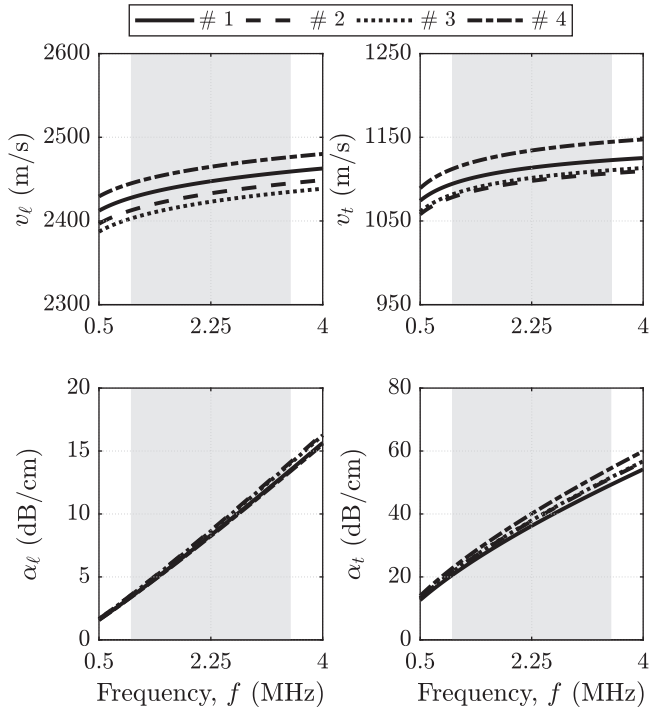


FIG. 5. Ultrasound characteristics, i.e., the phase velocity,  $v_r(\omega)$ , and the attenuation,  $\alpha_r(\omega)$ , obtained for three measurements performed on the same VW100 sample (#1, #2, #3) and one measurement on a thinner VW100 sample (#4). The light gray areas display the useful frequency bandwidth of the probe on which the inversion was conducted.

readability of Fig. 6, only one out of the three measurements performed on VW100 was arbitrarily chosen, i.e., measurement #1. As expected, the optimized Szabo parameters,  $\mathbf{p}_r$ , are closely related to the volume fraction of VW. Indeed, when the volume fraction of VW decreases (from 100% to 0%), the phase velocity decreases, and the attenuation increases. In particular, the optimized longitudinal parameters, i.e.,  $[v_{cl}, \alpha_{cl}]$ , range from  $[2447 \pm 0.2 \text{ m/s}, 8.31 \pm 0.01 \text{ dB/cm}]$  for VW100 to  $[2035.1 \pm 0.9 \text{ m/s}, 15.4 \pm 0.03 \text{ dB/cm}]$  for EB100 (recall Table I). A similar trend is observed for the transverse parameters, i.e.,  $[v_{ct}, \alpha_{ct}]$ , where optimized values range from  $[1134.2 \pm 0.4 \text{ m/s}, 40.1 \pm 0.1 \text{ dB/cm}]$  to  $[740.6 \pm 0.8 \text{ m/s}, 86.3 \pm 1.5 \text{ dB/cm}]$ . Overall, it can be observed that the transverse phase velocity,  $v_t$ , is around two to three times lower than  $v_l$ , depending on the volume fraction of VW.

### C. Dispersive properties of photopolymer materials

As displayed in Fig. 5, the longitudinal (respectively, transverse) phase velocity,  $v_l$  (respectively,  $v_t$ ), increases nearly 50 m/s (respectively, 40 m/s) over the useful frequency bandwidth (i.e., 0.75–3.75 MHz). Likewise, the longitudinal (respectively, transverse) attenuation,  $\alpha_l$  (respectively,  $\alpha_t$ ), increases from 3 dB/cm to nearly 15 dB/cm (respectively, from 12 dB/cm to 70 dB/cm). Interestingly, the dispersion of the longitudinal and transverse characteristics, which depends on  $\alpha_{cr}$  and  $y_r$ , is similar for all samples, no matter whether they consist of pure or composite materials (see Fig. 6).

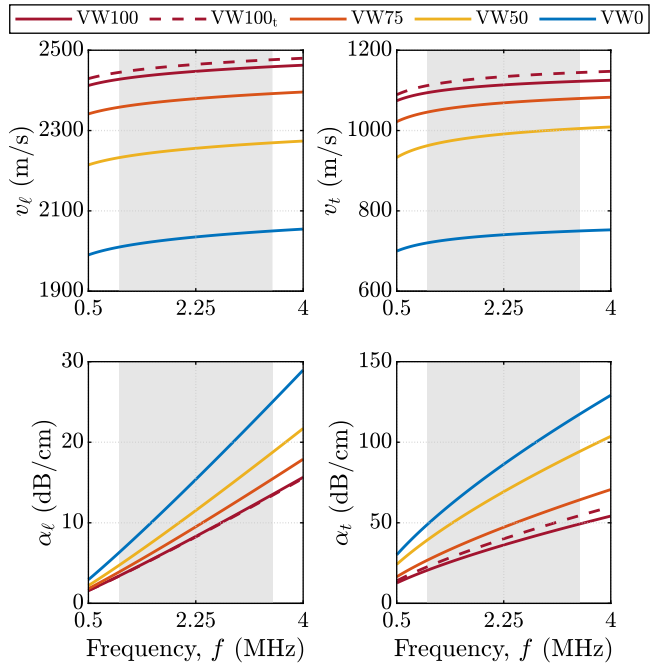


FIG. 6. (Color online) Ultrasound characteristics, i.e., the phase velocity,  $v_r(\omega)$ , and the attenuation,  $\alpha_r(\omega)$ , of VW100 (red), VW75 (orange), VW50 (yellow), and EB100 (blue) samples. The light gray areas display the useful frequency bandwidth of the probe on which the inversion was conducted.

## VI. DISCUSSION

The objective of the present work was to provide a methodological framework to identify the frequency-dependent viscoelastic properties in the MHz regime and the thickness of highly attenuating samples. Toward this goal, angular measurements achieved in double through-transmission were conducted on different photopolymer samples, which were obtained using multi-material AM. A direct modeling of the double through-transmission, based on a global matrix formalism, was proposed along with an inverse procedure, which altogether allowed inferring frequency-dependent ultrasound characteristics.

The proposed framework presents several advantages. First, in contrast to the approach used in Ref. 16, the experimental input consisted of the raw temporal signals (i.e., angular measurements) achieved in double through-transmission. Thereby, no signal processing steps were required to isolate the echoes of interest to compute their respective complex spectra such as signal windowing or phase unwrapping. In addition, the use of a reference signal (i.e., a double through-transmitted signal through water only) allowed weighting the measurements by the input signal bandwidth, thereby preventing any frequency range to be manually selected. A further advantage of using this reference signal was that the distances between the probe, sample, and mirror could be considered to be unknown. Second, the use of global matrix formalism for the modeling of the double through-transmitted signals allowed retrieving temporal  $\theta$ -scans, which could be systematically compared to the measurements to identify the ultrasound characteristics. In addition, the use of a rheological

model, such as the Szabo model, allowed identifying frequency-dependent properties with a reduced set of model parameters. Third, all the investigated parameters, including both ultrasound characteristics (phase velocity and attenuation of longitudinal and transverse waves) and the sample's thickness, were simultaneously optimized. In particular, an original initialization strategy using Prony's series decomposition was proposed, which is based on the measurement achieved in normal incidence. Altogether, this study provides a deeper insight on the ultrasound characteristics of state-of-the-art photopolymers commonly used for Polyjet printing purposes and, in particular, their transverse properties, which characterization remained challenging for such attenuating materials. To the best of our knowledge, the transverse properties of the soft elastomer (EB) investigated herein have not been reported in the ultrasonic regime so far.

The longitudinal bulk properties of the glassy polymer (VW) and soft elastomer (EB) were in good qualitative agreement with those reported in previous studies for photopolymer materials achieved with similar AM technologies.<sup>9,10,16</sup> Nonetheless, it is not straightforward to quantitatively compare the results of the present work with the literature because (i) the photopolymers may slightly differ across studies (their commercial names change and their compositions are unknown), and (ii) the material properties are not necessarily evaluated in the same frequency range, whereas it has been shown that such photopolymer materials exhibit a frequency-dependent behavior. On one hand, the longitudinal phase velocity of VW-like samples reported in the literature range from 2464 to 2495 m/s at a central frequency of about 2.25 MHz.<sup>10,15,16</sup> Likewise, the values of the longitudinal attenuation of VW reported herein (recall Table I) are also in close agreement with those of the literature, which range from 7.6 to 8.2 dB/cm.<sup>15,16</sup> On the other hand, Ref. 10 reported longitudinal bulk properties close to 2040 m/s and 18.4 dB/cm for Agilus30, which is a soft elastomer similar to EB, used for 3D printing purposes with the Polyjet technology.

In the same way, the transverse bulk properties reported by Ref. 16 for a VW-like sample with a phase velocity of  $1112.9 \pm 4.5$  m/s and attenuation of  $37.9 \pm 0.5$  dB/cm are in very good agreement with those obtained herein (recall Table I). While the transverse properties of EB have not been reported so far, Ref. 16 investigated a composite material made of VW and an intermediate volume fraction up to 18% of a soft elastomer (TangoBlack<sup>TM</sup>), a photopolymer also used for 3D printing with Polyjet technology. The properties obtained for this material are consistent with our VW75 sample (intermediate volume fraction equal to 25% of EB) with a transverse phase velocity equal to  $1066.2 \pm 3.7$  m/s (VW75,  $1069.1 \pm 0.2$ ) and an attenuation of  $48.8 \pm 0.6$  dB/cm (VW75,  $47.2 \pm 0.2$  dB/cm).

Overall, the reported properties are all in very good agreement with those of the literature, thereby confirming the robustness of the proposed inverse identification procedure based on ultrasonic angular measurements achieved in double through-transmission. Moreover, the values of the sample thickness concurrently obtained from the optimization are very close to the reference values with less than 5%

of relative error, which is consistent with the resolution of the caliper ( $\pm 0.02$  mm). Eventually, it is worth mentioning the possible effects of the water—and, thus, the sample—temperature, which could explain the small discrepancies observed.<sup>35</sup> Despite these promising results, our approach suffers from some limitations. First, some discrepancies were observed over the three measurement repetitions performed on the VW100 samples as well as between the two VW100 samples with different thicknesses (recall Fig. 5). The inter- and intra-sample reproducibilities, which are of the same order of magnitude and lower than 5% for the phase velocities,  $v_{cr}$ , and attenuations,  $\alpha_{cr}$ , were significantly higher than the uncertainty associated with the inverse procedure. Such variations may be related to a misalignment of the probe/mirror or parallelism/curvature of the sample and could be minimized by improving the experimental setup and manufacturing process. These may also be caused by small variations across the prints, for instance, as a result of different sample positioning on the building tray. Eventually, as mentioned by the manufacturer, the samples are prone to water absorption (e.g., 1%–1.2% for the VW), which could slightly modify the effective properties of the samples once immersed, thereby explaining the small discrepancy between the two VW100 samples with different thicknesses (recall Fig. 5). Second, the number of investigated samples is relatively low and further composite samples with intermediate volume fractions should be incorporated in future studies with the aim of establishing mixing rules for these materials in the ultrasonic regime.

Altogether, this study provides an original framework to retrieve the frequency-dependent ultrasound characteristics of dissimilar viscoelastic materials, ranging from glassy polymer to soft elastomer. The properties reported here are of significant interest toward applications requiring a precise knowledge of the longitudinal and transverse bulk properties of such materials in the MHz regime as, for instance, the modeling of the wave interactions with multi-material architected media.<sup>14</sup> A next step will be to generalize the identification procedure to other kinds of polymers and anisotropic media. In this respect, the use of a phenomenological model to describe the dispersion and attenuation relation will be avoided. To this end, the measurements will be performed on a larger frequency range, and the inversion will be performed for each frequency. Likewise, the versatility of design at different scales (from micro to macro) offered by multi-material AM strengthens the need to account for anisotropy in further works.

## ACKNOWLEDGMENT

This work was supported by the “Coup de pouce 2022” of the *Fédération Francilienne de Mécanique* (F2M) for young researchers.

## AUTHOR DECLARATIONS

### Conflict of Interest

The authors have no conflicts to disclose.

## DATA AVAILABILITY

The data that support the findings of this study are openly available in Theta-scan, Ref. 36.

## APPENDIX A: GLOBAL MATRIX FORMALISM

In the two fluid subdomains ( $|x| > h/2$ ), the Helmholtz equation governing the pressure field accepts two plane wave solutions, corresponding to the forward *incident*,  $a_{\text{I}}$ , and *transmitted*,  $a_{\text{T}} \equiv a_0^+$ , waves with  $\xi_{\text{I}} = \xi_{\text{T}} = \chi_0$  and the backward *reflected* wave,  $a_{\text{R}} \equiv a_0^-$ , with  $\xi_{\text{R}} = -\chi_0$  [see Eq. (7)]. In the isotropic solid subdomain ( $|x| < h/2$ ), the 2D Navier-Cauchy equations apply, which accept two solution pairs of backward and forward waves defined by  $\xi_r = \pm \chi_r$  and corresponding to *longitudinal* ( $r = \ell$ ) and *transverse* ( $r = t$ ) motion associated, respectively, with

$$k_\ell^2 = \chi_\ell^2 + \kappa^2 = \omega^2 \frac{\rho}{\lambda + 2\mu}, \quad \mathbf{U}^{(\ell)} = \frac{1}{\omega^2} \begin{bmatrix} \xi_r \\ \kappa \end{bmatrix}, \quad (\text{A1a})$$

$$k_t^2 = \chi_t^2 + \kappa^2 = \omega^2 \frac{\rho}{\mu}, \quad \mathbf{U}^{(t)} = \frac{1}{\omega^2} \begin{bmatrix} -\kappa \\ \xi_r \end{bmatrix}, \quad (\text{A1b})$$

where  $(\lambda, \mu)$  are the Lamé coefficients and the scaling of the wave polarization vectors,  $\mathbf{U}^{(r)}$ , where  $\omega$  has been introduced to simplify the derivations. Using Hooke's law to express the local stress vector as a function of the elementary waves in the solid, the six continuity equations in Eq. (5) (three equations on two interfaces) can be recast as the following system:

$$\begin{aligned} & \sum_{r=\{0,\ell,t\}} \begin{bmatrix} z_r \mathcal{B}^{(r^+)} & z_r^{-1} \mathcal{B}^{(r^-)} \\ z_r^{-1} \mathcal{B}^{(r^+)} & z_r \mathcal{B}^{(r^-)} \end{bmatrix} \begin{bmatrix} a_r^+ \\ a_r^- \end{bmatrix} \\ & = -a_{\text{I}} \begin{bmatrix} z_0 \mathcal{B}^{(0^+)} \\ \mathbf{0} \end{bmatrix}, \\ & \mathcal{B}^{(r)} = \begin{bmatrix} \rho \omega^2 [\xi_r k_t^2 \mathcal{U}_1^{(r)} + \kappa(k_t^2 - 2k_\ell^2) \mathcal{U}_2^{(r)}] \\ + i k_\ell^2 k_t^2 \mathcal{P}^{(r)} \\ \rho \omega^2 k_\ell^2 (\kappa \mathcal{U}_1^{(r)} + \xi_r \mathcal{U}_2^{(r)}) \\ \rho_0 \omega^2 \mathcal{U}_1^{(r)} + i \xi_r \mathcal{P}^{(r)} \end{bmatrix}, \end{aligned} \quad (\text{A2})$$

where  $z_r = e^{i(h/2)\chi_r}$  with  $r = \ell, t, 0$ . Notice that  $a_{\text{I}}$ , as the source term, has been placed on the right side. The symmetry of the forward-backward waves (given by  $\xi_r = \pm \chi_r$ ) and the symmetry of the solid-fluid interfaces (located at  $x = \pm h/2$ ) are taken into account by the change of variables  $a_r^\pm = a_r^S \pm a_r^A$ , the use of  $c_r = \cos(h/2)\chi_r$  and  $s_r = \sin(h/2)\chi_r$ , and the vectors  $\mathcal{S}^{(r)} = \mathcal{B}^{(r^+)} + \mathcal{B}^{(r^-)}$  and  $\mathcal{A}^{(r)} = \mathcal{B}^{(r^+)} - \mathcal{B}^{(r^-)}$  with few nonzero coefficients:

$$\mathcal{S}_1^{(0)} = 2i(\chi_t^2 + \kappa^2), \quad \mathcal{A}_3^{(0)} = 2i\chi_0,$$

$$\mathcal{S}_1^{(\ell)} = \mathcal{S}_2^{(t)} = 2\rho(\chi_t^2 - \kappa^2), \quad \mathcal{S}_3^{(t)} = -2\rho_0\kappa,$$

$$\mathcal{A}_1^{(t)} = -4\rho\kappa\chi_t, \quad \mathcal{A}_2^{(\ell)} = 4\rho\kappa\chi_\ell, \quad \mathcal{A}_3^{(\ell)} = 2\rho_0\chi_\ell.$$

Altogether, this allows rewriting Eq. (A2) as two smaller systems of uncoupled equations:

$$\begin{bmatrix} z_0^{-1} \mathcal{S}_1^{(0)} & 2c_\ell \mathcal{S}_1^{(\ell)} & 2c_t \mathcal{A}_1^{(t)} \\ 0 & 2s_\ell \mathcal{A}_2^{(\ell)} & 2s_t \mathcal{S}_2^{(t)} \\ iz_0^{-1} \mathcal{A}_3^{(0)} & 2s_\ell \mathcal{A}_3^{(\ell)} & 2s_t \mathcal{S}_3^{(t)} \end{bmatrix} \begin{bmatrix} a_0^S \\ a_\ell^S \\ a_t^S \end{bmatrix} = \begin{bmatrix} -z_0 \mathcal{B}_1^{(0^+)} \\ 0 \\ iz_0 \mathcal{B}_3^{(0^+)} \end{bmatrix} a_{\text{I}}, \quad (\text{A3})$$

$$\begin{bmatrix} -iz_0^{-1} \mathcal{S}_1^{(0)} & 2s_\ell \mathcal{S}_1^{(\ell)} & 2s_t \mathcal{A}_1^{(t)} \\ 0 & 2c_\ell \mathcal{A}_2^{(\ell)} & 2c_t \mathcal{S}_2^{(t)} \\ z_0^{-1} \mathcal{A}_3^{(0)} & 2c_\ell \mathcal{A}_3^{(\ell)} & 2c_t \mathcal{S}_3^{(t)} \end{bmatrix} \begin{bmatrix} a_0^A \\ a_\ell^A \\ a_t^A \end{bmatrix} = \begin{bmatrix} -iz_0 \mathcal{B}_1^{(0^+)} \\ 0 \\ -z_0 \mathcal{B}_3^{(0^+)} \end{bmatrix} a_{\text{I}}, \quad (\text{A4})$$

which can be inverted to finally obtain

$$a_\ell^S = \frac{z_0^2}{2} a_{\text{I}} \frac{(\alpha c_\ell s_t + \beta s_\ell c_t) - i\gamma s_\ell s_t}{(\alpha c_\ell s_t + \beta s_\ell c_t) + i\gamma s_\ell s_t}, \quad (\text{A5})$$

$$a_0^A = \frac{z_0^2}{2} a_{\text{I}} \frac{\gamma c_\ell c_t - i(\alpha s_\ell c_t + \beta c_\ell s_t)}{\gamma c_\ell c_t + i(\alpha s_\ell c_t + \beta c_\ell s_t)}, \quad (\text{A6})$$

where  $\alpha$ ,  $\beta$ , and  $\gamma$  are given in Eq. (9).

## APPENDIX B: INITIALIZATION

The expression of the inverse double-transmitted wave transfer given in Eq. (14) is a harmonic polynomial in which poles,  $(\psi_\ell^{-\omega}, 1, \psi_\ell^\omega)$ , can be estimated after compensation of the water-related phase,  $\psi_0^\omega$ . More predominantly, it is well-known from Prony's works that the data samples,  $h_n = \psi_0^{-\omega} H_{2\text{T}}^{-1}(n\Delta\omega)$ , are related by the following recurrence relation:

$$0 = h_{n+3} + \sum_{m=0}^2 p_m h_{n+m}, \quad (\text{B1})$$

and the roots of the polynomial,  $P(\pi)$ , formed by the coefficients,  $p_m$ , are the signal poles,

$$\begin{aligned} P(\pi) &= \pi^3 + \sum_{m=0}^2 p_m \pi^m \\ &= (\pi - \psi_\ell^{-\Delta\omega})(\pi - 1)(\pi - \psi_\ell^{\Delta\omega}). \end{aligned} \quad (\text{B2})$$

Hence, the recurrence relation takes the form

$$(h_{n+3} - h_n) - p_2(h_{n+2} - h_{n+1}) = 0, \quad (\text{B3})$$

$$p_2 = (\psi_\ell^{\Delta\omega} + \psi_\ell^{-\Delta\omega} + 1) = 2 \cos \frac{2h\Delta\omega}{v_\ell} + 1. \quad (\text{B4})$$

The coefficient,  $p_2$ , can be estimated from the normal incidence data,  $\mathbf{h} = [h_1 \dots h_N]$ , using weighted least squares, where the chosen weight takes into account the input signal bandwidth. At the end, the initial frequency-independent longitudinal wave speed is obtained as

$$v_\ell = \frac{2h\Delta\omega}{\text{acos}\left(\frac{p_2 - 1}{2}\right)}. \quad (\text{B5})$$

- <sup>1</sup>N. Li, S. Huang, G. Zhang, R. Qin, W. Liu, H. Xiong, G. Shi, and J. Blackburn, "Progress in additive manufacturing on new materials: A review," *J. Mater. Sci. Technol.* **35**(2), 242–269 (2019).
- <sup>2</sup>A. du Plessis, C. Broeckhoven, I. Yadroitsava, I. Yadroitsev, C. H. Hands, R. Kunju, and D. Bhate, "Beautiful and functional: A review of biomimetic design in additive manufacturing," *Addit. Manuf.* **27**, 408–427 (2019).
- <sup>3</sup>A. Velasco-Hogan, J. Xu, and M. A. Meyers, "Additive manufacturing as a method to design and optimize bioinspired structures," *Adv. Mater.* **30**(52), 1800940 (2018).
- <sup>4</sup>G. Dong, D. Tessier, and Y. F. Zhao, "Design of shoe soles using lattice structures fabricated by additive manufacturing," *Proc. Int. Conf. Eng. Des.* **1**(1), 719–728 (2019).
- <sup>5</sup>Y. Zhang, M.-T. Hsieh, and L. Valdevit, "Mechanical performance of 3D printed interpenetrating phase composites with spinodal topologies," *Compos. Struct.* **263**, 113693 (2021).
- <sup>6</sup>M. J. Mirzaali, M. Cruz Saldívar, A. Herranz de la Nava, D. Gunashekar, M. Nouri-Goushki, E. L. Doubrovski, and A. A. Zadpoor, "Multi-material 3D printing of functionally graded hierarchical soft-hard composites," *Adv. Eng. Mater.* **22**(7), 1901142 (2020).
- <sup>7</sup>A. R. Studart, "Additive manufacturing of biologically-inspired materials," *Chem. Soc. Rev.* **45**(2), 359–376 (2016).
- <sup>8</sup>J. Giannatsis and V. Dedoussis, "Additive fabrication technologies applied to medicine and health care: A review," *Int. J. Adv. Manuf. Technol.* **40**, 116–127 (2007).
- <sup>9</sup>J.-R. Jacquet, F. Ossant, F. Levassort, and J.-M. Gregoire, "3-D-printed phantom fabricated by photopolymer jetting technology for high-frequency ultrasound imaging," *IEEE Trans. Ultrason, Ferroelect., Freq. Contr.* **65**(6), 1048–1055 (2018).
- <sup>10</sup>M. Bakaric, P. Miloro, A. Javaherian, B. T. Cox, B. E. Treeby, and M. D. Brown, "Measurement of the ultrasound attenuation and dispersion in 3D-printed photopolymer materials from 1 to 3.5 MHz," *J. Acoust. Soc. Am.* **150**(4), 2798–2805 (2021).
- <sup>11</sup>M. Ferri, J. M. Bravo, J. Redondo, S. Jiménez-Gambín, N. Jiménez, F. Camarena, and J. V. Sánchez-Pérez, "On the evaluation of the suitability of the materials used to 3D print holographic acoustic lenses to correct transcranial focused ultrasound aberrations," *Polymers* **11**(9), 1521 (2019).
- <sup>12</sup>A. Tikhonov, P. Evdokimov, E. Klimashina, S. Tikhonova, E. Karpushkin, I. Scherbackov, V. Dubrov, and V. Putlayev, "Stereolithographic fabrication of three-dimensional permeable scaffolds from CaP/PEGDA hydrogel biocomposites for use as bone grafts," *J. Mech. Behav. Biomed. Mater.* **110**, 103922 (2020).
- <sup>13</sup>M. Gattin, N. Bochud, G. Rosi, Q. Grossman, D. Ruffoni, and S. Naili, "Ultrasonic bandgaps in viscoelastic 1D-periodic media: Mechanical modeling and experimental validation," *Ultrasonics* **131**, 106951 (2023).
- <sup>14</sup>M. Gattin, N. Bochud, Q. Grossman, D. Ruffoni, G. Rosi, and S. Naili, "Ultrasound monitoring of multiphase architected media: Bandgap tracking via the measurement of the reflection coefficient," *Appl. Acoust.* **217**, 109844 (2024).
- <sup>15</sup>A. Aghaei, N. Bochud, G. Rosi, Q. Grossman, D. Ruffoni, and S. Naili, "Ultrasound characterization of bioinspired functionally graded soft-to-hard composites: Experiment and modeling," *J. Acoust. Soc. Am.* **151**(3), 1490–1501 (2022).
- <sup>16</sup>M. Gattin, N. Bochud, G. Rosi, Q. Grossman, D. Ruffoni, and S. Naili, "Ultrasound characterization of the viscoelastic properties of additively manufactured photopolymer materials," *J. Acoust. Soc. Am.* **152**(3), 1901–1912 (2022).
- <sup>17</sup>S. I. Rokhlin and W. Wang, "Double through-transmission bulk wave method for ultrasonic phase velocity measurement and determination of elastic constants of composite materials," *J. Acoust. Soc. Am.* **91**(6), 3303–3312 (1992).
- <sup>18</sup>Y. C. Chu and S. I. Rokhlin, "Comparative analysis of through-transmission ultrasonic bulk wave methods for phase velocity measurements in anisotropic materials," *J. Acoust. Soc. Am.* **95**(6), 3204–3212 (1994).
- <sup>19</sup>D. Zhou, L. Peirlinckx, and L. Van Biesen, "Identification of parametric models for ultrasonic double transmission experiments on viscoelastic plates," *J. Acoust. Soc. Am.* **99**(3), 1446–1458 (1996).
- <sup>20</sup>M. Castaings, B. Hosten, and T. Kundu, "Inversion of ultrasonic, plane-wave transmission data in composite plates to infer viscoelastic material properties," *NDT&E Int.* **33**(6), 377–392 (2000).
- <sup>21</sup>B. Hosten, "Reflection and transmission of acoustic plane waves on an immersed orthotropic and viscoelastic solid layer," *J. Acoust. Soc. Am.* **89**(6), 2745–2752 (1991).
- <sup>22</sup>L. Peirlinckx, P. Guillaume, R. Pintelon, and L. Van Biesen, "A global system identification approach for the accurate parametric modeling of ultrasonic reflection and transmission experiments," *IEEE Trans. Ultrason, Ferroelect., Freq. Contr.* **43**(4), 628–639 (1996).
- <sup>23</sup>B. Hosten and M. Castaings, "Comments on the ultrasonic estimation of the viscoelastic properties of anisotropic materials," *Compos. Part A Appl. Sci. Manuf.* **39**(6), 1054–1058 (2008).
- <sup>24</sup>A. I. Lavrentyev and S. I. Rokhlin, "Determination of elastic moduli, density, attenuation, and thickness of a layer using ultrasonic spectroscopy at two angles," *J. Acoust. Soc. Am.* **102**(6), 3467–3477 (1997).
- <sup>25</sup>E. Siryabe, M. Rénier, A. Meziane, J. Galy, and M. Castaings, "Apparent anisotropy of adhesive bonds with weak adhesion and non-destructive evaluation of interfacial properties," *Ultrasonics* **79**, 34–51 (2017).
- <sup>26</sup>L. Zorretto, L. Andena, F. Briatico-Vangosa, L. De Noni, J.-M. Thomassin, C. Jérôme, Q. Grossman, A. Mertens, R. Weinkamer, M. Rink, and D. Ruffoni, "Properties and role of interfaces in multimaterial 3D printed composites," *Sci. Rep.* **10**(1), 22285 (2020).
- <sup>27</sup>D. Royer and E. Dieulesaint, *Elastic Waves in Solids I: Free and Guided Propagation* (Springer Science and Business Media, Berlin, Germany, 1999).
- <sup>28</sup>S. Catheline, J.-L. Gennisson, G. Delon, M. Fink, R. Sinkus, S. Abouelkaram, and J. Culioli, "Measurement of viscoelastic properties of homogeneous soft solid using transient elastography: An inverse problem approach," *J. Acoust. Soc. Am.* **116**(6), 3734–3741 (2004).
- <sup>29</sup>W. Marczak, "Water as a standard in the measurements of speed of sound in liquids," *J. Acoust. Soc. Am.* **102**(5), 2776–2779 (1997).
- <sup>30</sup>P. He, "Direct measurement of ultrasonic dispersion using a broadband transmission technique," *Ultrasonics* **37**(1), 67–70 (1999).
- <sup>31</sup>A. H. Nayfeh, "The general problem of elastic wave propagation in multi-layered anisotropic media," *J. Acoust. Soc. Am.* **89**(4), 1521–1531 (1991).
- <sup>32</sup>T. L. Szabo and J. Wu, "A model for longitudinal and shear wave propagation in viscoelastic media," *J. Acoust. Soc. Am.* **107**(5), 2437–2446 (2000).
- <sup>33</sup>M. O'Donnell, E. T. Jaynes, and J. G. Miller, "Kramers-Kronig relationship between ultrasonic attenuation and phase velocity," *J. Acoust. Soc. Am.* **69**(3), 696–701 (1981).
- <sup>34</sup>S. Guo, M. Rébillat, and N. Mechbal, "Prediction of frequency and spatially dependent attenuation of guided waves propagating in mounted and unmounted A380 parts made up of anisotropic viscoelastic composite laminates," *Struct. Health. Monit.* **22**(2), 1326–1352 (2023).
- <sup>35</sup>Q. Baudis, T. Valier-Brasier, and R. Wunenburger, "Thorough ultrasonic rheology of soft, visco-elastic materials: Example of crosslinked Polyurethane elastomer," *Ultrasonics* **137**, 107166 (2024).
- <sup>36</sup>A.-S. Poudrel, P. Margerit, and N. Bochud, "Theta-scan," <https://zenodo.org/records/11102338>.